Article

Tuning the Chern number in quantum anomalous Hall insulators

https://doi.org/10.1038/s41586-020-3020-3

Received: 28 June 2020

Accepted: 2 October 2020

Published online: 16 December 2020

Check for updates

Yi-Fan Zhao[1,3], Ruoxi Zhang[1,3], Ruobing Mei[1,3], Ling-Jie Zhou[1], Hemian Yi[1], Ya-Qi Zhang[1], Jiabin Yu[1], Run Xiao[1], Ke Wang[2], Nitin Samarth[1], Moses H. W. Chan[1], Chao-Xing Liu[1]✉ & Cui-Zu Chang[1]✉

A quantum anomalous Hall (QAH) state is a two-dimensional topological insulating state that has a quantized Hall resistance of $h/(Ce^2)$ and vanishing longitudinal resistance under zero magnetic field (where h is the Planck constant, e is the elementary charge, and the Chern number C is an integer)[1,2]. The QAH effect has been realized in magnetic topological insulators[3–9] and magic-angle twisted bilayer graphene[10,11]. However, the QAH effect at zero magnetic field has so far been realized only for $C = 1$. Here we realize a well quantized QAH effect with tunable Chern number (up to $C = 5$) in multilayer structures consisting of alternating magnetic and undoped topological insulator layers, fabricated using molecular beam epitaxy. The Chern number of these QAH insulators is determined by the number of undoped topological insulator layers in the multilayer structure. Moreover, we demonstrate that the Chern number of a given multilayer structure can be tuned by varying either the magnetic doping concentration in the magnetic topological insulator layers or the thickness of the interior magnetic topological insulator layer. We develop a theoretical model to explain our experimental observations and establish phase diagrams for QAH insulators with high, tunable Chern number. The realization of such insulators facilitates the application of dissipationless chiral edge currents in energy-efficient electronic devices, and opens up opportunities for developing multi-channel quantum computing and higher-capacity chiral circuit interconnects.

The Chern number, also known as the Thouless–Kohmoto–Nightingale–Nijs (TKNN) number, is an integer that defines the topological phase in the quantum Hall effect[12]. It is calculated as the integral of the Berry curvature over the entire first Brillouin zone and determines the number of topologically protected chiral edge channels along the edge of a sample[13]. The QAH effect may be considered as the quantum Hall effect under zero magnetic field and can be realized in a time-reversal symmetry-breaking system with the inverted electronic band structure[1,2,14,15]. The QAH effect under zero magnetic field has so far been realized in only three systems: (1) molecular beam epitaxy (MBE)-grown magnetically doped topological insulator films, such as Cr- and/or V-doped $(Bi,Sb)_2Te_3$ (refs. [3,4,6–9]); (2) mechanically exfoliated intrinsic magnetic topological insulator $MnBi_2Te_4$ thin flakes with an odd number of layers[5]; and (3) manually assembled twisted bilayer graphene[10,11]. The QAH states observed in these systems were limited to $C = 1$. In $C = 1$ QAH insulators, the chiral edge current is dissipationless, but the contact resistance between the normal metal electrodes and the chiral edge channels is limited to a minimum value ($h/(Ce^2)$), set by Landauer–Büttiker theory[16,17]. This contact resistance constrains even proof-of-concept device technologies that may seek to take advantage of chiral edge channel transport. A solution is to greatly reduce the contact resistance by increasing the number of parallel chiral edge channels in QAH devices, with an effective Hall resistance of $h/(Ce^2)$ for high C[18,19]. Larger C also increases the effective breakdown current of chiral edge states and thus facilitates the practical applications of QAH devices. A $C = 2$ Chern insulator has recently been realized under a finite external magnetic field, but without well-defined Landau levels, in thin $MnBi_2Te_4$ flakes[20] and in a rhombohedral trilayer graphene–hexagonal boron nitride moiré superlattice[21]. Here, we report the realization of high-C QAH insulators (with C tunable to integer values up to 5) with good quantization and vanishing longitudinal resistance at zero magnetic field.

The high-C QAH effect has been theoretically proposed in Cr-doped $Bi_2(Se,Te)_3$ (ref. [18]) and magnetically doped topological crystalline insulator SnTe (ref. [19]) films. The high-C QAH effect in the former system is predicted when two or more pairs of inverted sub-bands are induced by strong exchange fields[18,22], whereas the high-C QAH effect in the latter system is conjectured in the presence of multiple Dirac surface states[19]. In practice, the realization of the high-C QAH state in Cr-doped $Bi_2(Se,Te)_3$ films for strong exchange fields is unlikely, owing to non-square or hysteresis-free loop and the possible metallic phase[23,24]. Realizing the high-C QAH state in magnetically doped SnTe is also challenging, owing to the absence of ferromagnetism and/or the fact that multiple Dirac points are normally located at different energies. These properties make it difficult to have a fully gapped surface in the SnTe system[19,25]. In addition to these two systems, the

[1]Department of Physics, The Pennsylvania State University, University Park, PA, USA. [2]Materials Research Institute, The Pennsylvania State University, University Park, PA, USA. [3]These authors contributed equally: Yi-Fan Zhao, Ruoxi Zhang, Ruobing Mei. ✉e-mail: cxl56@psu.edu; cxc955@psu.edu

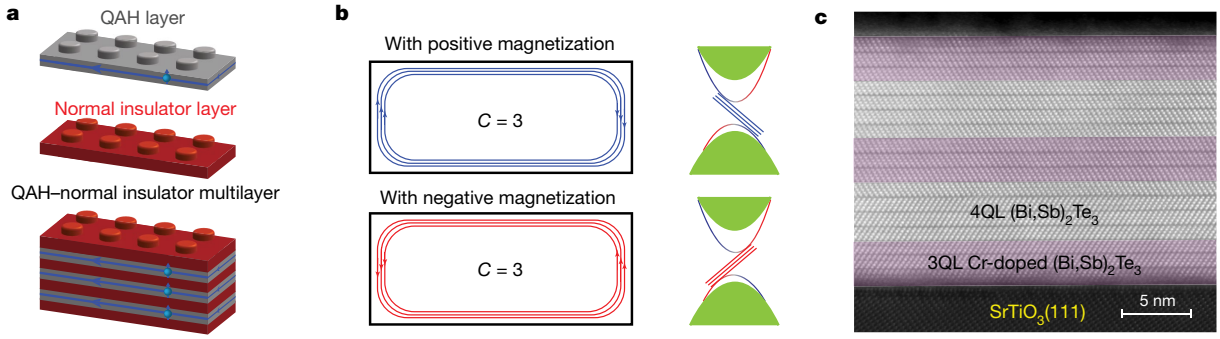

Fig. 1 | The high-*C* QAH effect in magnetic–undoped topological insulator multilayer structures. a, Schematics of the high-*C* QAH insulator in *C* = 1 QAH–normal insulator multilayer structures. The blue arrows illustrate the chiral edge channels of the QAH insulators. **b**, Schematics of the high-*C* QAH effect. We take a *C* = 3 QAH insulator as an example. Three chiral edge channels are shown in real space (left) and momentum space (right) for positive (top) and negative (bottom) magnetization. **c**, Cross-sectional STEM image of the *m* = 2 multilayer structure grown on a $SrTiO_3$ substrate.

high-*C* QAH state may also be realized in magnetic topological insulator multilayer structures with alternating *C* = 1 QAH and normal insulator layers (Fig. 1a)[26]. The thickness of the normal insulator layer modulates the coupling between two *C* = 1 QAH layers and thus tunes the Chern number of QAH multilayer samples. Experimental efforts in this direction have demonstrated the possibility of having multiple QAH layers connected in parallel using insulating CdSe layers. Because CdSe has a wurtzite structure, which is different from the tetradymite structure of magnetic topological insulators, stacking faults inevitably arise in QAH–CdSe multilayer samples. These defects might be responsible for the reported large longitudinal resistance and Hall resistances greater than the corresponding quantized values[27].

High-*C* QAH effect

Similar to *C* = 1 QAH insulators[3–10], high-*C* QAH insulators harbour *C* dissipationless chiral edge channels[18,19]. These edge states are spin-polarized and their chirality is determined by the internal magnetization of the sample (Fig. 1b). In our alternating magnetic–undoped topological insulator multilayer structures, the heavily Cr-doped $(Bi,Sb)_2Te_3$ layer (x = 0.24 in $(Bi,Sb)_{2-x}Cr_xTe_3$) has two roles. First, its magnetism breaks the time-reversal symmetry of the 4 quintuple layer (QL) $(Bi,Sb)_2Te_3$ layer and thus allows the *C* = 1 QAH effect to emerge in the 3QL $(Bi,Sb)_{1.76}Cr_{0.24}Te_3$–4QL $(Bi,Sb)_2Te_3$–3QL $(Bi,Sb)_{1.76}Cr_{0.24}Te_3$ structure (Fig. 2a). Second, the bulk bandgap of the magnetic topological insulator layer may become non-inverted because the heavy Cr doping greatly reduces the spin–orbit coupling of the system[23,24]. In addition, the Chern number of our multilayer structures can be determined by the strength of the coupling between two adjacent *C* = 1 QAH layers—that is, by the thickness of the interior magnetic topological insulator layers. High-*C* QAH insulators emerge when this coupling is weak (when the magnetic topological insulator layer is thick). When the coupling is stronger than a critical value (when the magnetic topological insulator is thin enough or absent), the sample exhibits a QAH state with *C* = 1. In Fig. 1c, we show a cross-sectional scanning transmission electron microscopy (STEM) image of the *m* = 2 multilayer sample, where *m* is the number of undoped topological insulator layers in the multilayers. Because the magnetically doped and undoped topological insulators have the same lattice structure, our samples have a highly ordered lattice structure (Extended Data Fig. 1). As we show in detail below, this structure is very important for realizing the tunable high-*C* QAH effect with good quantization.

We carried out magneto-transport measurements on [3QL $(Bi,Sb)_{1.76}Cr_{0.24}Te_3$–4QL $(Bi,Sb)_2Te_3]_m$–3QL $(Bi,Sb)_{1.76}Cr_{0.24}Te_3$ ($1 \le m \le 5$) multilayer samples at T = 25 mK, with the bottom gate voltage V_g tuned at the charge neutral point $V_{g,0}$ (Fig. 2). All five samples exhibit the QAH effect, with varying degrees of quantization precision and longitudinal resistance minima. For the *m* = 1 sample, the Hall resistance ρ_{yx} has a quantized value of $0.994h/e^2$, and the longitudinal resistance ρ_{xx} is $0.0001h/e^2$ (about 2.5 Ω) under zero magnetic field, corresponding to a QAH state with *C* = 1 (Fig. 2a). By inserting one more period of the 3QL $(Bi,Sb)_{1.76}Cr_{0.24}Te_3$–4QL $(Bi,Sb)_2Te_3$ bilayer (*m* = 2 sample), ρ_{yx} displays a quantized value of $0.498h/e^2$, and ρ_{xx} is $0.008h/e^2$ under zero magnetic field, giving rise to a QAH state with *C* = 2 (Fig. 2b). After inserting more periods of the 3QL $(Bi,Sb)_{1.76}Cr_{0.24}Te_3$–4QL $(Bi,Sb)_2Te_3$ bilayers, ρ_{yx} displays quantized values of $0.329h/e^2$, $0.234h/e^2$ and $0.185h/e^2$ (*m* = 3, 4 and 5 samples, respectively). The corresponding values of ρ_{xx} in these samples are $0.022h/e^2$, $0.039h/e^2$ and $0.044h/e^2$ under zero magnetic field (Fig. 2c–e). These are QAH states with *C* = 3, 4 and 5. We speculate that the increasing value of ρ_{xx} under zero magnetic field with increasing number of periods in the multilayer samples probably comes from three sources. First, conduction from the dissipative quasi-helical side surface states increases in thicker samples[17,28]; second, conduction from the dissipative residual bulk carriers increases in thicker samples; and third, tuning the chemical potentials of two surfaces simultaneously into magnetic exchange gaps via a single bottom gate V_g becomes harder in thicker QAH samples[29]. Further studies are needed to clarify which source is dominant in these thick multilayer samples.

The realization of high-*C* QAH insulators (*C* = 1–5) in magnetic–undoped topological insulator multilayer structures is further validated by the V_g dependence of ρ_{yx} and ρ_{xx} at zero magnetic field ($\rho_{yx}(0)$ and $\rho_{xx}(0)$; Fig. 3). In all five samples, $\rho_{yx}(0)$ exhibits distinct plateaus at the quantized value $h/(Ce^2)$, centred at $V_g = V_{g,0}$. Accompanying the quantization in $\rho_{yx}(0)$, $\rho_{xx}(0)$ is greatly suppressed for the *m* = 1–5 samples (Fig. 3). The ratio $\rho_{yx}(0)/\rho_{xx}(0)$ corresponds to anomalous Hall angles of 89.99°, 89.08°, 86.17°, 80.54° and 76.55° for the *m* = 1–5 samples, respectively. Here, we define the critical temperature of the high-*C* QAH state as that at which $\rho_{yx}(0)/\rho_{xx}(0) = 1$ (the crossing point between the $\rho_{yx}(0)$–T and $\rho_{xx}(0)$–T curves in Extended Data Figs. 2–6). The critical temperatures are 3.5 K, 2.6 K, 8.3 K, 6.7 K and 6.3 K for the *C* = 1–5 samples, respectively.

Tuning the Chern number in QAH insulators

We show that the Chern numbers of these QAH insulators can be tuned by controlling either the magnetic doping concentration in the magnetic topological insulator layers or the thickness of the interior magnetic topological insulator layers. We first systematically change the Cr doping concentration in the *m* = 2 sample ([3QL $(Bi,Sb)_{2-x}Cr_xTe_3$–4QL $(Bi,Sb)_2Te_3]_2$–3QL $(Bi,Sb)_{2-x}Cr_xTe_3$). Similarly to the *m* = 2 sample with x = 0.24 (Figs. 2b, 3b), the sample with a higher Cr doping concentration (x = 0.35) shows the *C* = 2 QAH effect with $\rho_{yx}(0) = 0.497h/e^2$. By contrast, the *m* = 2 samples with lower Cr doping concentrations (x = 0.13 and x = 0.15) exhibit the *C* = 1 QAH effect, with $\rho_{yx}(0) = 0.969h/e^2$ for the

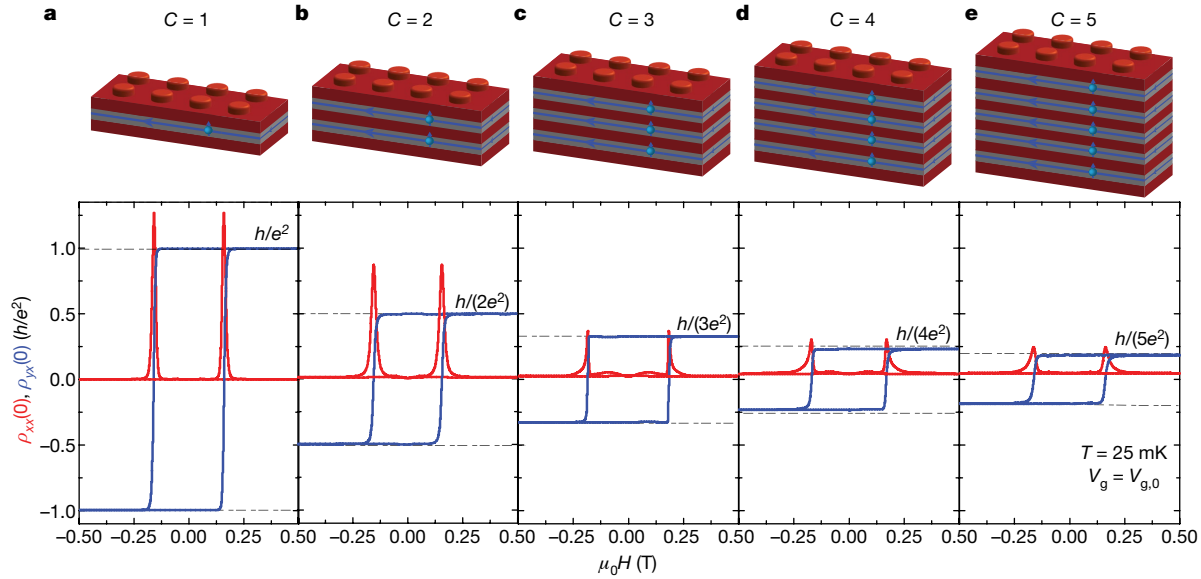

Fig. 2 | Observations of the high-*C* QAH effect in magnetic–undoped topological insulator multilayer structures. a–**e**, Top, schematics of the multilayer structures for the QAH effect with $C = 1$ to $C = 5$. Bottom, dependence of the longitudinal resistance ρ_{xx} (red) and the Hall resistance ρ_{yx} (blue) on the magnetic field $\mu_0 H$, measured at the charge-neutral point ($V_g = V_{g,0}$) and $T = 25$ mK. $V_{g,0}$ values for the five samples are +11 V ($C = 1$), +10 V ($C = 2$), +2 V ($C = 3$), +2 V ($C = 4$) and −3 V ($C = 5$). The thicknesses of the five samples are 10 nm ($C = 1$), 17 nm ($C = 2$), 24 nm ($C = 3$), 31 nm ($C = 4$) and 38 nm ($C = 5$).

$x = 0.13$ sample and $\rho_{yx}(0) = 0.996h/e^2$ for the $x = 0.15$ sample (Fig. 4a). Such a change in C from 2 to 1 occurs in the $m = 2$ samples because lowering the Cr concentration not only drives the bulk energy gap of the magnetic topological insulator layers towards the inverted (nontrivial) regime[23,24] but also reduces their spin splitting from exchange coupling[2,13,14]. As a result, nontrivial interface states disappear at the interfaces between the interior magnetic and undoped topological insulator layers with decreasing Cr concentration, so only a pair of nontrivial interface states localized at the top and bottom magnetic topological insulator layers of the $m = 2$ sample contributes to the total Hall resistance ($C = 1$; Fig. 4c). For higher Cr doping concentrations, the spin–orbit coupling of the magnetic topological insulator layer is weakened and this layer tends to become a trivial insulator layer, while the exchange spin splitting is enhanced. Consequently, two nontrivial interface states are formed at the interface between the interior magnetic and undoped topological insulator layers, which results in two pairs of nontrivial interface states contributing to the total Hall resistance ($C = 2$; Fig. 4c).

We next changed the thickness d of the middle magnetic topological insulator layer in the $m = 2$ sample ([3QL $(Bi,Sb)_{1.76}Cr_{0.24}Te_3$–4QL $(Bi,Sb)_2Te_3$]–dQL $(Bi,Sb)_{1.76}Cr_{0.24}Te_3$–[4QL $(Bi,Sb)_2Te_3$–3QL $(Bi,Sb)_{1.76}Cr_{0.24}Te_3$]) to modulate the coupling between two $C = 1$ QAH layers. For $d = 0$ and $d = 1$, the coupling between the top and bottom two QAH layers is strong and only a pair of nontrivial interface states exist (Fig. 4c); consequently, these two samples show the $C = 1$ QAH effect. Indeed, $\rho_{yx}(0)$ is quantized at $0.995h/e^2$ for $d = 0$ and at $0.996h/e^2$ for $d = 1$ (Fig. 4b). For $d \geq 2$, the interaction between the top and bottom QAH layers is reduced and one more pair of nontrivial interface states emerges (Fig. 4c), resulting in the $C = 2$ QAH effect. In this case, $\rho_{yx}(0)$ is quantized at $0.469h/e^2$ for $d = 2$ and at $0.491h/e^2$ for $d = 4$ (Fig. 4b).

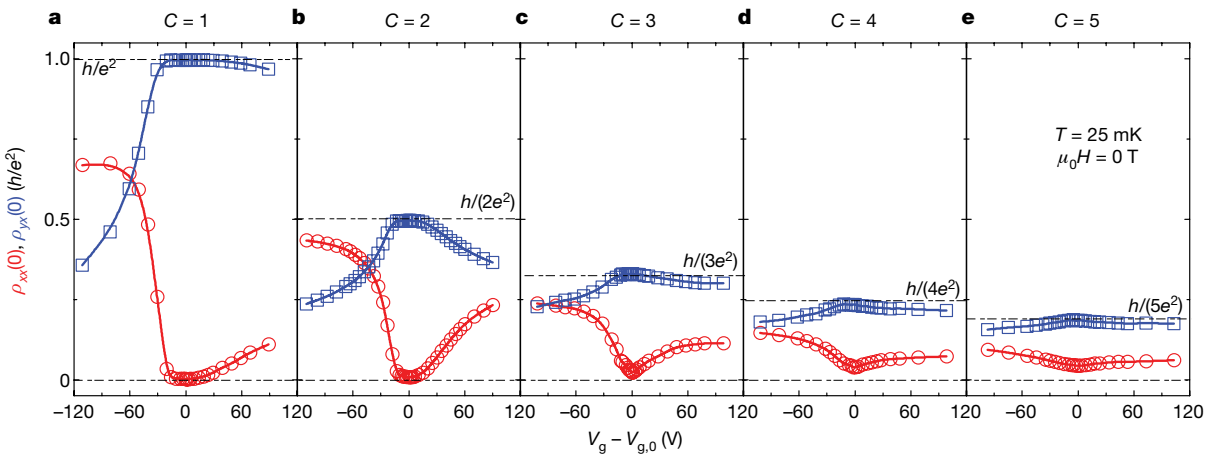

Fig. 3 | Demonstration of high-*C* QAH states in magnetic–undoped topological insulator multilayer structures. a–**e**, Dependence of $\rho_{yx}(0)$ (blue squares) and $\rho_{xx}(0)$ (red circles) on gate voltage ($V_g - V_{g,0}$) for QAH insulators with $C = 1$ to $C = 5$. All measurements were taken at $T = 25$ mK and $\mu_0 H = 0$ T after magnetic training.

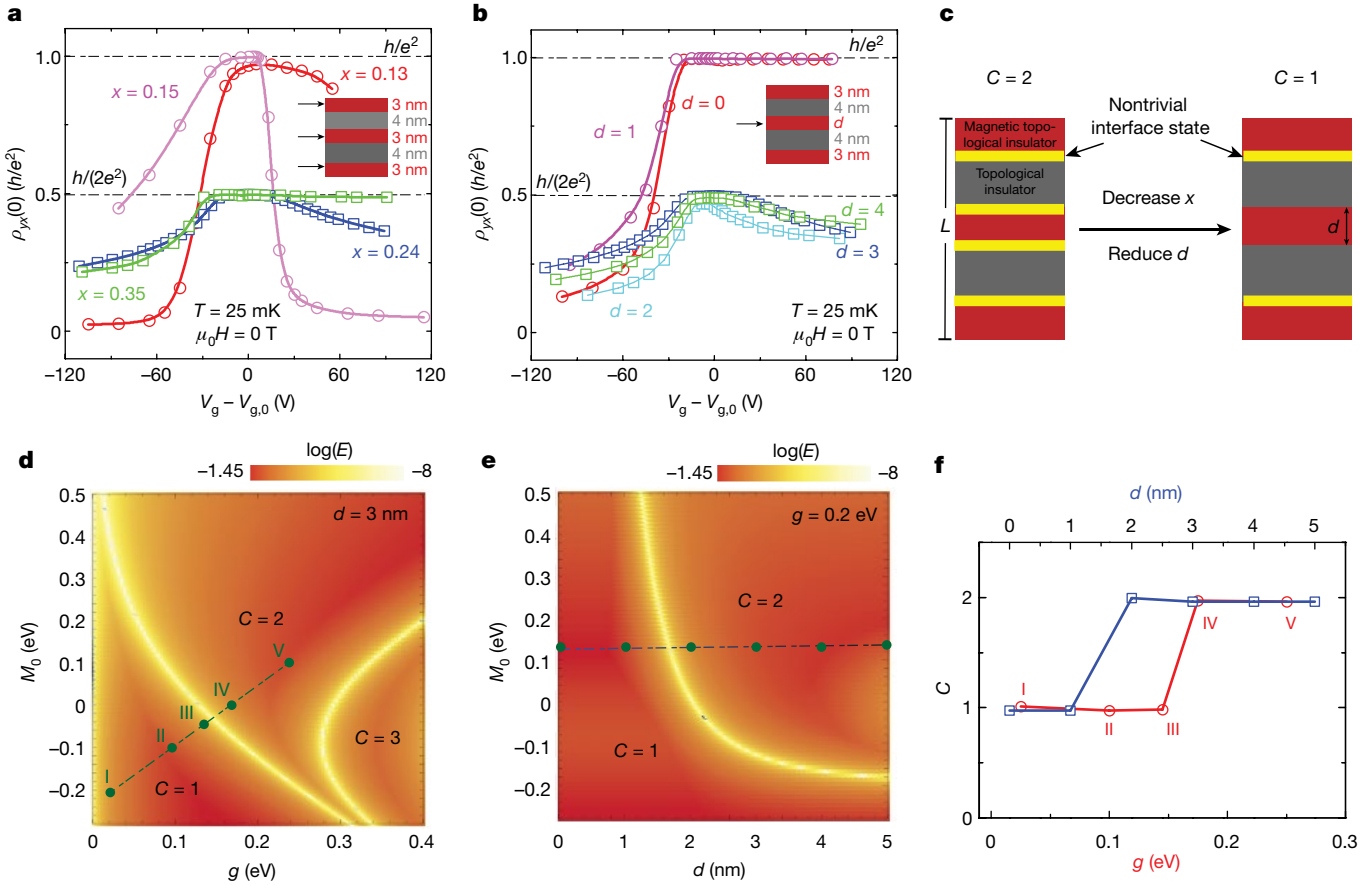

Fig. 4 | Tunable Chern number in QAH insulators. a, Dependence of $\rho_{yx}(0)$ on gate voltage ($V_g - V_{g,0}$) for the $m = 2$ samples ([3QL $(Bi,Sb)_{2-x}Cr_xTe_3$–4QL $(Bi,Sb)_2Te_3$]$_2$–3QL $(Bi,Sb)_{2-x}Cr_xTe_3$), with different Cr doping concentration x. The samples with $x = 0.13$ or $x = 0.15$ exhibit the $C = 1$ QAH effect, whereas the samples with $x = 0.24$ or $x = 0.35$ exhibit the $C = 2$ QAH effect. $V_{g,0}$ values for the four samples are +65 V ($x = 0.13$), −10 V ($x = 0.15$), +10 V ($x = 0.24$) and +9 V ($x = 0.35$). **b**, Dependence of $\rho_{yx}(0)$ on gate voltage ($V_g - V_{g,0}$) for the $m = 2$ samples ([3QL $(Bi,Sb)_{1.76}Cr_{0.24}Te_3$–4QL $(Bi,Sb)_2Te_3$]–dQL $(Bi,Sb)_{1.76}Cr_{0.24}Te_3$–[4QL $(Bi,Sb)_2Te_3$–3QL $(Bi,Sb)_{1.76}Cr_{0.24}Te_3$]), with varying the thickness of the middle magnetic topological insulator layer d. The samples with $d = 0$ or $d = 1$ samples exhibit the $C = 1$ QAH effect, whereas the samples with $d = 2$, $d = 3$ or $d = 4$ exhibit the $C = 2$ QAH effect. $V_{g,0}$ values for the four samples are +20 V ($d = 0$), +23 V ($d = 1$), +18 V ($d = 2$), +10 V ($d = 3$) and +4 V ($d = 4$). **c**, Schematics of nontrivial interface states (yellow) in the $m = 2$ sample, which can be tuned by controlling x and d. A pair of nontrivial interface states adds one to the total Chern number. **d**, Calculated phase diagram for the $m = 2$ sample as a function of the gap parameter M_0 and the exchange coupling parameter g of the Cr-doped topological insulator layers. M_0 and g both change with x in the magnetic topological insulator layers. **e**, Calculated phase diagram for the $m = 2$ sample as a function of the thickness d and the gap parameter M_0 of the middle Cr-doped topological insulator layer. In **d** and **e**, the colour scale indicates the magnitude of $\log(E)$, where E is the calculated energy gap of the $m = 2$ heterostructure sample. **f**, Calculated Chern number C for all points shown in **d** (points I–V; red, bottom axis) and **e** ($d = 0$–5 nm; blue, top axis).

Theoretical simulation

To support our interpretation, we numerically simulated the magnetic–undoped topological insulator multilayer structures using a four-band model[30] with Hamiltonian

$$H(\mathbf{k}_{\|}, -i\partial_z) = \varepsilon(\mathbf{k}_{\|}, -i\partial_z) + M(\mathbf{k}_{\|}, -i\partial_z)\tau_z + B(-i\partial_z)\tau_y + A(k_y\tau_x\sigma_x - k_x\tau_x\sigma_y) + g(z)\sigma_z,$$

where

$$\varepsilon(\mathbf{k}_{\|}, -i\partial_z) = C_0 + C_1(-\partial_z^2) + C_2k_{\|}^2,$$

$$M(\mathbf{k}_{\|}, -i\partial_z) = \mathcal{M}_0(z) + M_1(-\partial_z^2) + M_2k_{\|}^2,$$

$\mathbf{k}_{\|} = (k_x, k_y)$ is the in-plane momentum, and C_0, C_1, C_2, $\mathcal{M}_0$, M_1, M_2, A, B and g are material-dependent parameters. $\mathcal{M}_0$ is the key parameter that characterizes the inverted ($\mathcal{M}_0 < 0$) and non-inverted ($\mathcal{M}_0 > 0$) band structures[31]. The Pauli matrices σ and τ represent spin and orbital degrees of freedom. To simulate multilayer structures with total multilayer thickness L, we considered the eigen-equation

$$H(\mathbf{k}_{\|}, -i\partial_z)\psi_{\mathbf{k}_{\|}}(z) = E\psi_{\mathbf{k}_{\|}}(z)$$

with open boundary condition $\psi_{\mathbf{k}_{\|}}(z = 0) = \psi_{\mathbf{k}_{\|}}(z = L) = 0$. We noted above that the Cr doping has two roles. First, it reduces the spin–orbit coupling of the magnetic topological insulator layers and drives their bulk energy gap towards the non-inverted insulator regime (described by $\mathcal{M}_0$)[23]. Second, it introduces magnetic moments in topological insulators, resulting in a spin splitting (described by g) due to the exchange coupling[2]. Consequently, we considered the z dependence of these parameters as

$$\mathcal{M}_0(z), g(z) = \begin{cases} M_0, g & z \in \text{Cr} - \text{doped topological insulator layer} \\ M_0', 0 & z \in \text{undoped topological insulator layer} \end{cases}.$$

We numerically solve the eigen-equation and compute the Hall conductance σ_{xy} (Methods). In the following, we focus on the $m = 2$ multilayer structure ($L = 17$ nm) to interpret the tunable Chern number observed in our experiments (Fig. 4a, b).

We first study the process of varying the Cr doping concentration. Because Cr dopants primarily affect the parameters M_0 and g in the magnetic topological insulator layers, we plot the bulk energy gap of the $m = 2$ multilayer structure as a function of M_0 and g (Fig. 4d). The energy-gap closing is depicted by the bright yellow lines, which separate different phases. The process of adding Cr dopants in our experiments qualitatively corresponds to moving from point I to point V along the dashed line in Fig. 4d, which shows that increasing the Cr doping concentration increases M_0 and g. Our calculation suggests that the Hall conductance σ_{xy} takes the value e^2/h for points I, II and III ($C = 1$) and $2e^2/h$ for points IV and V ($C = 2$), qualitatively reproducing the influence of Cr doping in our experiments (Fig. 4a).

Our simulation provides more insights into the physical mechanism. We find that the Hall conductance σ_{xy} comes predominantly from the interface Dirac bands, that is, the bands that have dispersions similar to those of gapped Dirac fermions and that are spatially localized at the interfaces between the magnetic and undoped topological insulator layers (Supplementary Fig. 5). For the $m = 2$ sample, there are four interfaces, two outer ones and two inner ones (Fig. 4c), and each interface possesses one occupied interface Dirac band. Because each interface Dirac band contributes $e^2/(2h)$ to the total Hall conductance σ_{xy}, four Dirac bands add up to $\sigma_{xy} = 2e^2/h$ ($C = 2$; Fig. 4c, f, Supplementary Fig. 5). On reducing the Cr doping concentration in the magnetic topological insulator layer, two sets of Dirac bands at two inner interfaces penetrate more into the bulk, leading to a gap closing and re-opening with a trivial hybridization gap. After this topological phase transition, the Hall conductance σ_{xy} comes only from the Dirac bands at two outer interfaces (Fig. 4c, f, Supplementary Fig. 6).

Next, we turn to the process of reducing the thickness d of the middle magnetic topological insulator layer in the $m = 2$ multilayer sample. As shown in Fig. 4e, reducing d may also induce the topological phase transition from $C = 2$ to $C = 1$ QAH insulators. With appropriate values of M_0 and g, our calculation indicates that the critical thickness value for the transition lies between 1 nm and 2 nm ($d = 1$ and $d = 2$), which coincided with our experimental observations of the change in Chern number in Fig. 4b.

To summarize, we fabricated alternating magnetic–undoped topological insulator multilayer structures and realized QAH insulators with Chern numbers of 1–5. The Chern number in the same sample configuration may be tuned by varying either the magnetic doping concentration in magnetic topological insulator layers or the thickness of the interior magnetic topological insulator layers. The realization of QAH insulators with tunable Chern number elucidates and expands the known topological phases of quantum matter. This advance also provides a platform for demonstrating proof-of-concept applications that exploit the dissipationless chiral edge current of QAH insulators. The greatly reduced contact resistance in high-C QAH devices allows information to be multiplexed over multiple chiral edge channels. The tuning of the Chern number in QAH insulators introduces the channel degree of freedom of chiral edge states and opens up the possibility of using topologically protected and dissipationless chiral edge states to store and transfer quantum information. Finally, magnetic–undoped topological insulator multilayers could enable the discovery and study of many other emergent topological phenomena, such as time-reversal-symmetry-breaking Weyl semimetal phases with only one pair of Weyl nodes[26] and axion electrodynamics[32,33].

Online content

Any methods, additional references, Nature Research reporting summaries, source data, extended data, supplementary information, acknowledgements, peer review information; details of author contributions and competing interests; and statements of data and code availability are available at https://doi.org/10.1038/s41586-020-3020-3.

1. Haldane, F. D. M. Model for a quantum Hall effect without Landau levels: condensed-matter realization of the "parity anomaly". *Phys. Rev. Lett.* **61**, 2015–2018 (1988).
2. Yu, R. et al. Quantized anomalous Hall effect in magnetic topological insulators. *Science* **329**, 61–64 (2010).
3. Chang, C. Z. et al. Experimental observation of the quantum anomalous Hall effect in a magnetic topological insulator. *Science* **340**, 167–170 (2013).
4. Chang, C. Z. et al. High-precision realization of robust quantum anomalous Hall state in a hard ferromagnetic topological insulator. *Nat. Mater.* **14**, 473–477 (2015).
5. Deng, Y. et al. Quantum anomalous Hall effect in intrinsic magnetic topological insulator. *Science* **367**, 895–900 (2020).
6. Kou, X. F. et al. Scale-invariant quantum anomalous Hall effect in magnetic topological insulators beyond the two-dimensional limit. *Phys. Rev. Lett.* **113**, 137201 (2014).
7. Checkelsky, J. G. et al. Trajectory of the anomalous Hall effect towards the quantized state in a ferromagnetic topological insulator. *Nat. Phys.* **10**, 731–736 (2014).
8. Mogi, M. et al. Magnetic modulation doping in topological insulators toward higher-temperature quantum anomalous Hall effect. *Appl. Phys. Lett.* **107**, 182401 (2015).
9. Ou, Y. et al. Enhancing the quantum anomalous Hall effect by magnetic codoping in a topological insulator. *Adv. Mater.* **30**, 1703062 (2018).
10. Serlin, M. et al. Intrinsic quantized anomalous Hall effect in a moiré heterostructure. *Science* **367**, 900–903 (2020).
11. Sharpe, A. L. et al. Emergent ferromagnetism near three-quarters filling in twisted bilayer graphene. *Science* **365**, 605–608 (2019).
12. Thouless, D. J. et al. Quantized Hall conductance in a two-dimensional periodic potential. *Phys. Rev. Lett.* **49**, 405–408 (1982).
13. Weng, H. M. et al. Quantum anomalous Hall effect and related topological electronic states. *Adv. Phys.* **64**, 227–282 (2015).
14. Liu, C. X. et al. Quantum anomalous Hall effect in $Hg_{1-y}Mn_yTe$ quantum wells. *Phys. Rev. Lett.* **101**, 146802 (2008).
15. Qi, X. L., Hughes, T. L. & Zhang, S. C. Topological field theory of time-reversal invariant insulators. *Phys. Rev. B* **78**, 195424 (2008).
16. Landauer, R. Spatial variation of currents and fields due to localized scatterers in metallic conduction. *IBM J. Res. Develop.* **1**, 223–231 (1957).
17. Chang, C. Z. et al. Zero-field dissipationless chiral edge transport and the nature of dissipation in the quantum anomalous Hall state. *Phys. Rev. Lett.* **115**, 057206 (2015).
18. Wang, J. et al. Quantum anomalous Hall effect with higher plateaus. *Phys. Rev. Lett.* **111**, 136801 (2013).
19. Fang, C., Gilbert, M. J. & Bernevig, B. A. Large-Chern-number quantum anomalous Hall effect in thin-film topological crystalline insulators. *Phys. Rev. Lett.* **112**, 046801 (2014).
20. Ge, J. et al. High-Chern-number and high-temperature quantum Hall effect without Landau levels. *Natl Sci. Rev.* **7**, 1280–1287 (2020).
21. Chen, G. R. et al. Tunable correlated Chern insulator and ferromagnetism in a moiré superlattice. *Nature* **579**, 56–61 (2020); publisher correction **581**, E3 (2020).
22. Jiang, H. et al. Quantum anomalous Hall effect with tunable Chern number in magnetic topological insulator film. *Phys. Rev. B* **85**, 045445 (2012).
23. Zhang, J. S. et al. Topology-driven magnetic quantum phase transition in topological insulators. *Science* **339**, 1582–1586 (2013).
24. Chang, C. Z. et al. Chemical-potential-dependent gap opening at the Dirac surface states of Bi_2Se_3 induced by aggregated substitutional Cr atoms. *Phys. Rev. Lett.* **112**, 056801 (2014).
25. Wang, F. et al. Chromium-induced ferromagnetism with perpendicular anisotropy in topological crystalline insulator SnTe (111) thin films. *Phys. Rev. B* **97**, 115414 (2018).
26. Burkov, A. A. & Balents, L. Weyl semimetal in a topological insulator multilayer. *Phys. Rev. Lett.* **107**, 127205 (2011).
27. Jiang, G. et al. Quantum anomalous Hall multilayers grown by molecular beam epitaxy. *Chin. Phys. Lett.* **35**, 076802 (2018).
28. Wang, J. et al. Anomalous edge transport in the quantum anomalous Hall state. *Phys. Rev. Lett.* **111**, 086803 (2013).
29. Feng, X. et al. Thickness dependence of the quantum anomalous Hall effect in magnetic topological insulator films. *Adv. Mater.* **28**, 6386–6390 (2016).
30. Liu, C. X. et al. Model Hamiltonian for topological insulators. *Phys. Rev. B* **82**, 045122 (2010).
31. Zhang, H. J. et al. Topological insulators in Bi_2Se_3, Bi_2Te_3 and Sb_2Te_3 with a single Dirac cone on the surface. *Nat. Phys.* **5**, 438–442 (2009).
32. Li, R. D. et al. Dynamical axion field in topological magnetic insulators. *Nat. Phys.* **6**, 284–288 (2010).
33. Wang, J., Lian, B. & Zhang, S. C. Dynamical axion field in a magnetic topological insulator superlattice. *Phys. Rev. B* **93**, 045115 (2016).

Methods

Growth of magnetic–undoped topological insulator (TI) multilayer structures

Magnetic TI/TI multilayer structures were fabricated in a commercial MBE system (Scienta Omicron Lab10) with a base pressure lower than 2×10^{-10} mbar. The insulating 0.25-mm $SrTiO_3$(111) substrates used for growth were first soaked in hot deionized water (about 80 °C) for 1.5 h and then annealed at 982 °C for 3 h in a tube furnace with flowing oxygen. Through this annealing process, the surface of $SrTiO_3$ substrates was passivated and atomically flat, suitable for the MBE growth of TI films. The heat-treated $SrTiO_3$(111) substrates were next loaded into the MBE chamber and outgassed at 600 °C for 1 h before the growth of magnetic TI/TI multilayer samples. High-purity Bi (99.999%), Sb (99.9999%), Cr (99.999%) and Te (99.9999%) were evaporated from Knudsen effusion cells. During the growth of the samples, the substrate was maintained at around 230 °C. The flux ratio of Te per (Bi + Sb + Cr) was set to greater than 10 to prevent Te deficiency in the films. The Bi/Sb ratio in each layer was optimized to tune the chemical potential for the entire multilayer near the charge-neutral point. The growth rate for the films was about 0.2QL per minute. Epitaxial growth was monitored by in situ reflection high-energy electron diffraction (RHEED) patterns, where the high crystal quality and the atomically flat surface were confirmed by the streaky and sharp 1 × 1 patterns (Extended Data Fig. 1b). No capping layer was involved in the ex situ electrical transport measurements.

Hall bar device fabrication

Magnetic TI/TI multilayer samples on 2 mm × 10 mm $SrTiO_3$(111) substrates were scratched into a Hall bar geometry using a computer-controlled probe station. The effective area of the Hall bar device is roughly 1 mm × 0.5 mm (Supplementary Fig. 1). The electrical ohmic contacts for transport measurements were made by pressing indium dots on the Hall bar. The bottom gate electrode was prepared by flattening indium spheres on the backside of the $SrTiO_3$ substrate.

Electrical transport measurements

Transport measurements were conducted using a Quantum Design Physical Property Measurement System (PPMS; 2 K, 9 T) and a Leiden Cryogenics dilution refrigerator (10 mK, 9 T), with the magnetic field applied perpendicular to the plane of the film. The bottom gate voltage V_g was applied using a Keithley 2450. The excitation currents used in the PPMS (≥2 K) and dilution (<2 K) measurements were 1 μA and 1 nA, respectively. The results reported here were reproduced on at least three samples for each Chern number (Extended Data Fig. 8). All magneto-transport results shown were symmetrized or anti-symmetrized as a function of the magnetic field to eliminate the effect of electrode misalignment. The raw data for Fig. 2 are shown in Supplementary Fig. 2. More transport results are provided in Extended Data Figs. 2–10.

Theoretical simulations and calculations

To numerically solve the eigen-equation for magnetic TI/TI multilayer structures, we expanded the wavefunction of the system as

$$\psi_{\mathbf{k}_\parallel}(z)=\sum_{n,\lambda}a_{n,\lambda}(\mathbf{k}_\parallel)\sqrt{\frac{2}{L}}\sin\left(\frac{n\pi z}{L}\right)|\lambda\rangle,$$

with the basis function

$$|n,\lambda\rangle=\sqrt{\frac{2}{L}}\sin\left(\frac{n\pi z}{L}\right)|\lambda\rangle,$$

where $\sin(n\pi z/L)$ satisfies the open boundary condition ($\psi_{\mathbf{k}_\parallel}(z=0)=\psi_{\mathbf{k}_\parallel}(z=L)=0$), $|\lambda\rangle$ is the basis of the four-band model, $a_{n,\lambda}(\mathbf{k}_\parallel)$ is the expansion coefficient, N is the overall normalization factor, and $n=1,\ldots,N$. From the eigen-equation and the expansion form, we obtain

$$\sum_{n',\lambda'}a_{n',\lambda'}\langle n,\lambda|H|n',\lambda'\rangle=Ea_{n,\lambda},$$

in which each matrix element is given by

$$\langle n,\lambda|H|n',\lambda'\rangle=\frac{2}{L}\int_0^L\sin\left(\frac{n\pi z}{L}\right)H_{\lambda\lambda'}(z)\sin\left(\frac{n'\pi z}{L}\right)\mathrm{d}z.$$

The parameters M_0 and g in the Hamiltonian matrix element $H_{\lambda\lambda'}$ take different values for the Cr-doped and undoped TI layers; thus, $H_{\lambda\lambda'}$ is z-dependent. In our calculations, we choose $\varepsilon=0$, $M_0'=-0.28$ eV, $M_1=6.86$ eV Å^2, $M_2=44.5$ eV Å^2, $A=3.33$ eV Å, $B=2.26$ eV Å and $N=50$. All these parameters are for Bi_2Se_3 from table 4 of ref. [30]. As examined in Supplementary Information, the energy dispersion obtained from this model describes our magnetic TI/TI multilayer samples well. We also did the same calculations using the parameters for Sb_2Te_3 (Supplementary Fig. 3) and found phase diagrams qualitatively similar to those shown in Fig. 4d, e.

To confirm the topological property of the system, we computed the Hall conductance σ_{xy} of a few points in Fig. 4d, e, using the Kubo formula

$$\sigma_{xy}=\frac{e^2}{h}\sum_{n\in\text{occupied}}C_{xy}(n)$$

and for the Chern number it is calculated by

$$C_{xy}(n)=\frac{1}{2\pi}\int\sum_m\frac{-\mathrm{i}(\langle\mathbf{u}_n|\partial_xH|\mathbf{u}_m\rangle\langle\mathbf{u}_m|\partial_yH|\mathbf{u}_n\rangle-\langle\mathbf{u}_n|\partial_yH|\mathbf{u}_m\rangle\langle\mathbf{u}_m|\partial_xH|\mathbf{u}_n\rangle)}{(\varepsilon_n-\varepsilon_m)^2}\mathrm{d}k_x\mathrm{d}k_y,$$

where $\partial_{x(y)}H=\partial H/\partial k_{x(y)}$, n and m denote the band index, and ε_n and $\mathbf{u}_n$ are the eigenvalue and eigenvector (corresponding to the periodic part of the Bloch state) for the nth band.

Data availability

The datasets generated and/or analysed during this study are available from the corresponding authors on reasonable request.

Code availability

The codes used in theoretical simulations and calculations are available from the corresponding authors on reasonable request.

Acknowledgements We are grateful to Y. T. Cui, J. Jain, W. D. Wu, D. Xiao and X. D. Xu for discussion. This work was primarily supported by a DOE grant (DE-SC0019064), including sample synthesis, transport measurements and theoretical calculations. The sample characterization was partially supported by an ARO Young Investigator Program Award (W911NF1810198), an NSF-CAREER award (DMR-1847811) and the Gordon and Betty Moore Foundation's EPiQS Initiative (GBMF9063 to C.Z.C.). Part of the measurements at dilution-refrigerator temperature is supported by NSF grant DMR-1707340. N.S. and R.X. acknowledge support from DOE EFRC grant DE-SC0019331.

Author contributions C.-Z.C. conceived and designed the experiment. Y.-F.Z., L.-J.Z. and Y.-Q.Z. grew the magnetic TI/TI multilayer samples and carried out the PPMS transport measurements, with help from C.-Z.C. K.W. performed the TEM measurements. R.Z., L.-J.Z. and Y.-Q.Z. carried out the dilution transport measurements, with help from M.H.W.C. and C.-Z.C. R.M., J.Y. and C.-X.L. did all calculations and provided theoretical support. Y.-F.Z., R.Z., R.M., C.-X.L. and C.-Z.C. analysed the data and wrote the manuscript, with input from all authors.

Competing interests The authors declare no competing interests.

Additional information
Supplementary information is available for this paper at https://doi.org/10.1038/s41586-020-3020-3.
Correspondence and requests for materials should be addressed to C.-X.L. or C.-Z.C.
Peer review information *Nature* thanks Xianhui Chen, Sanfeng Wu and the other, anonymous, reviewer(s) for their contribution to the peer review of this work. Peer reviewer reports are available.
Reprints and permissions information is available at http://www.nature.com/reprints.

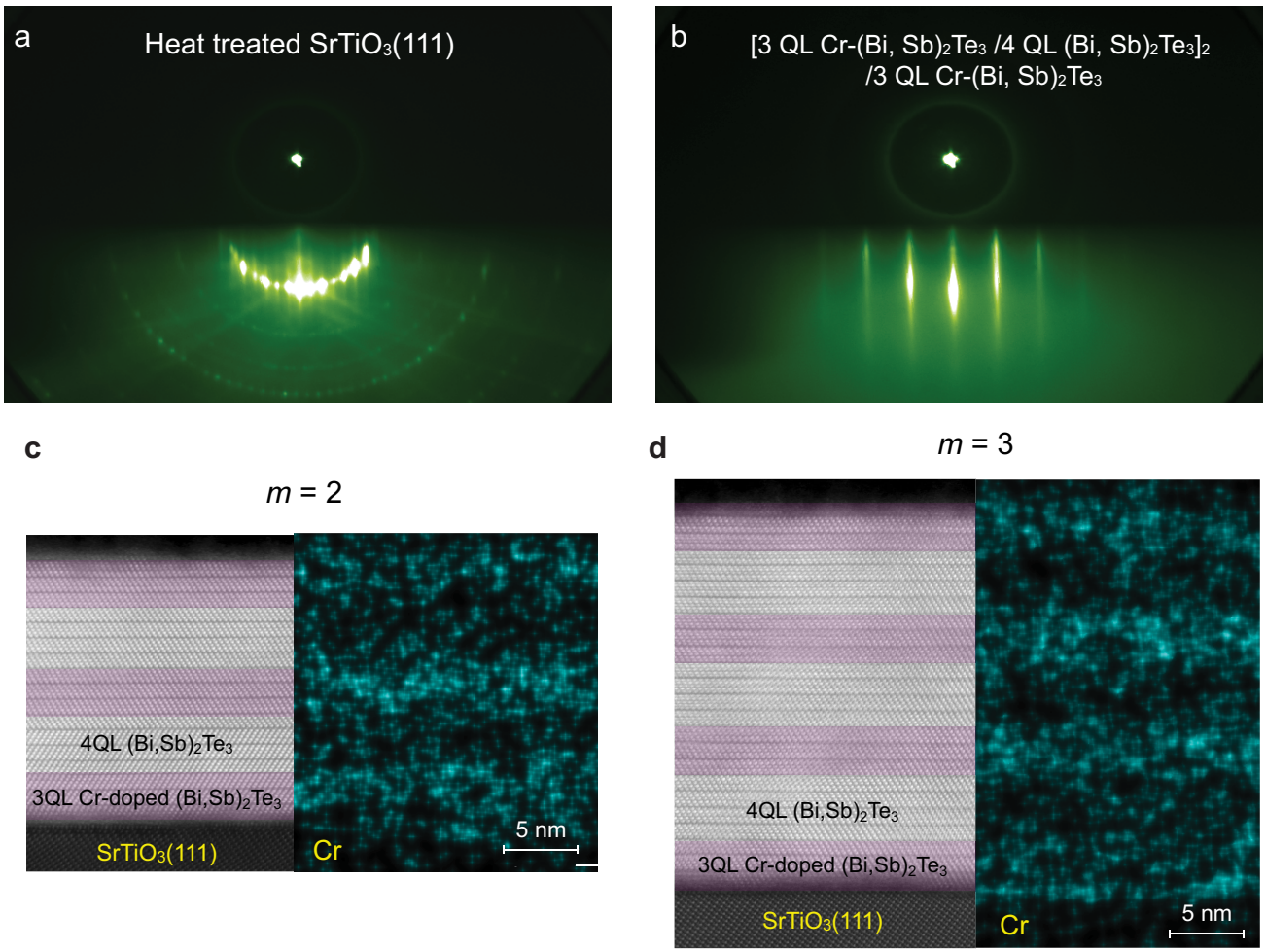

Extended Data Fig. 1 | Characterization of magnetic TI/TI multilayer samples. a, RHEED patterns of the heat-treated $SrTiO_3(111)$ substrate. The reconstruction pattern indicates its atomic flat surface, which is crucial for the MBE growth of the high-quality TI films. **b**, RHEED patterns of the [3QL Cr-doped $(Bi,Sb)_2Te_3$–4QL $(Bi,Sb)_2Te_3]_2$–3QL Cr-doped $(Bi,Sb)_2Te_3$ sample. The sharp and streaky 1 × 1 patterns indicate the high quality of our magnetic TI/TI multilayer samples. **c**, **d**, STEM images of the $m = 2$ (**c**) and $m = 3$ (**d**) magnetic TI/TI multilayer samples grown on $SrTiO_3$ substrate (left), accompanied by the energy-dispersive spectroscopy maps of Cr distribution (right).

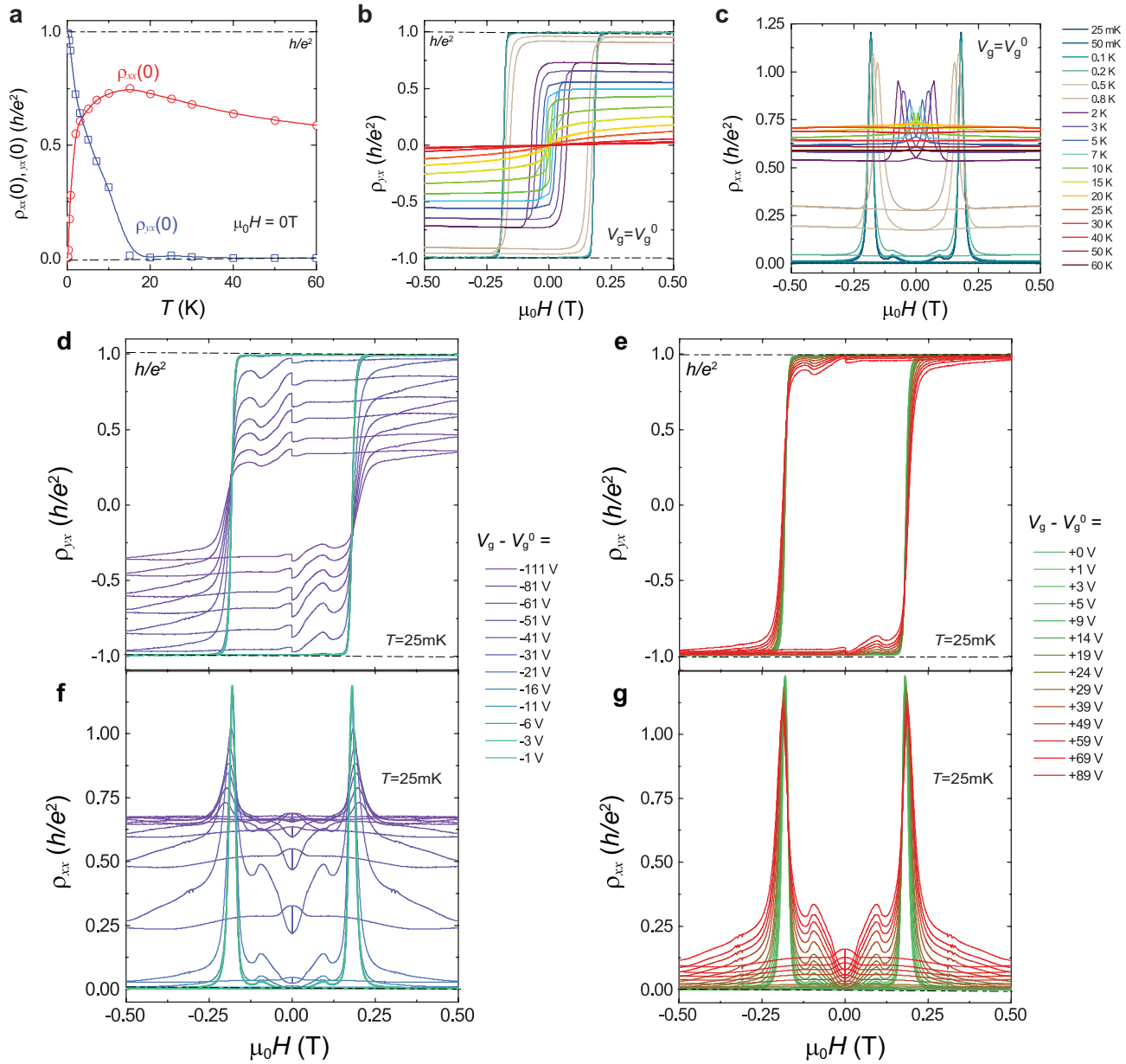

Extended Data Fig. 2 | Transport results for the *C* = 1 sample. a, Dependence of $\rho_{yx}(0)$ (blue squares) and $\rho_{xx}(0)$ (red circles) on T. All measurements were taken at $\mu_0 H = 0$ T after magnetic training. **b**, **c**, Dependence of ρ_{yx} (**b**) and ρ_{xx} (**c**) on $\mu_0 H$, measured at different temperatures and $V_g = V_{g,0}$. **d**–**g**, Dependence of ρ_{yx} (**d**, **e**) and ρ_{xx} (**f**, **g**) on $\mu_0 H$, measured at different gate voltages (**d**, **f**, $V_g < V_{g,0}$; **e**, **g**, $V_g \geq V_{g,0}$) and $T = 25$ mK. When V_g is tuned away from $V_{g,0}$, ρ_{yx} and ρ_{xx} show additional transition features once the external magnetic field changes the polarity. We speculate that these features are probably a result of the heating generated in the dilution fridge and/or the indium contacts used in our samples.

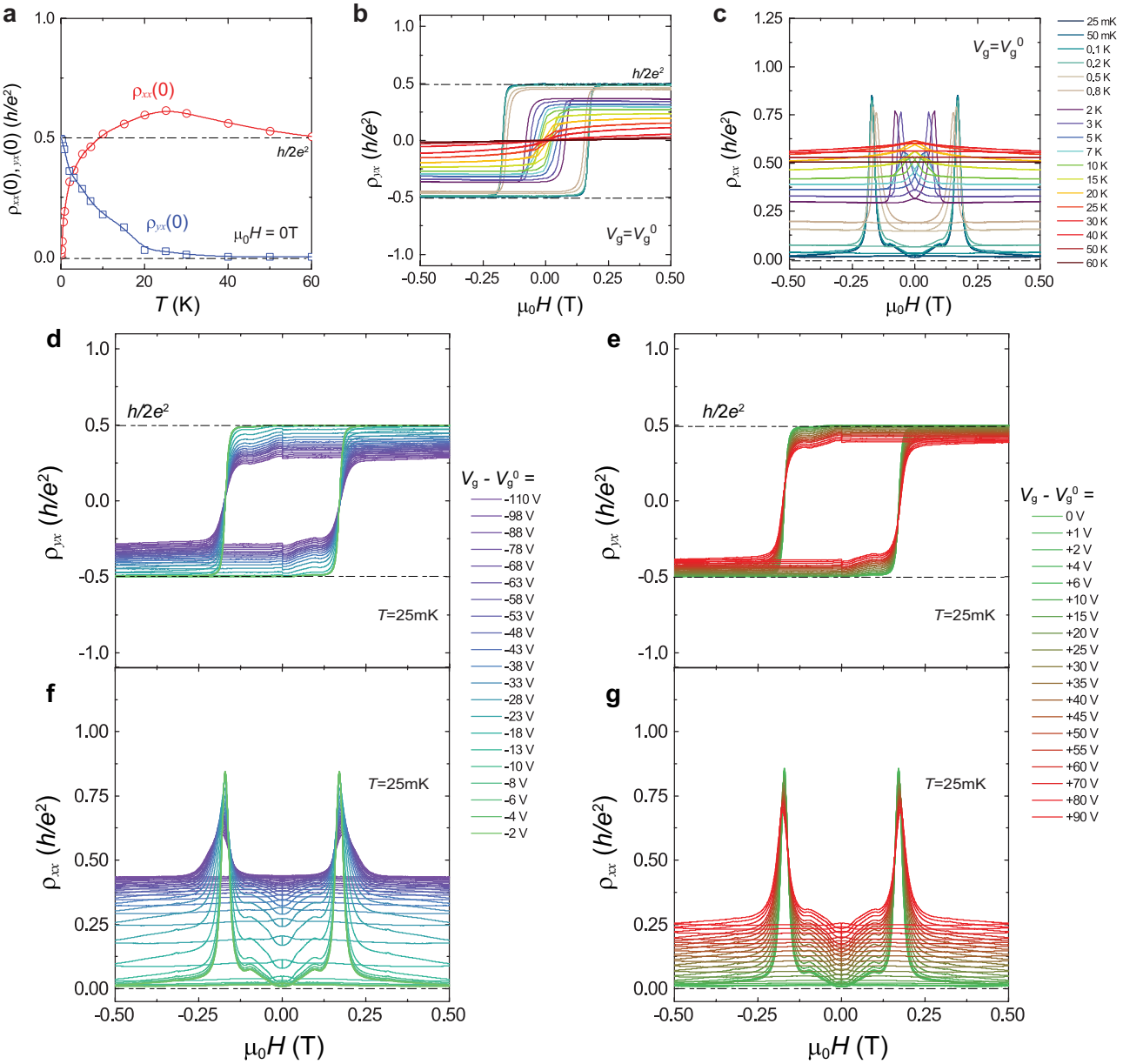

Extended Data Fig. 3 | Transport results for the $C = 2$ sample. As in Extended Data Fig. 2, but for the $C = 2$ sample.

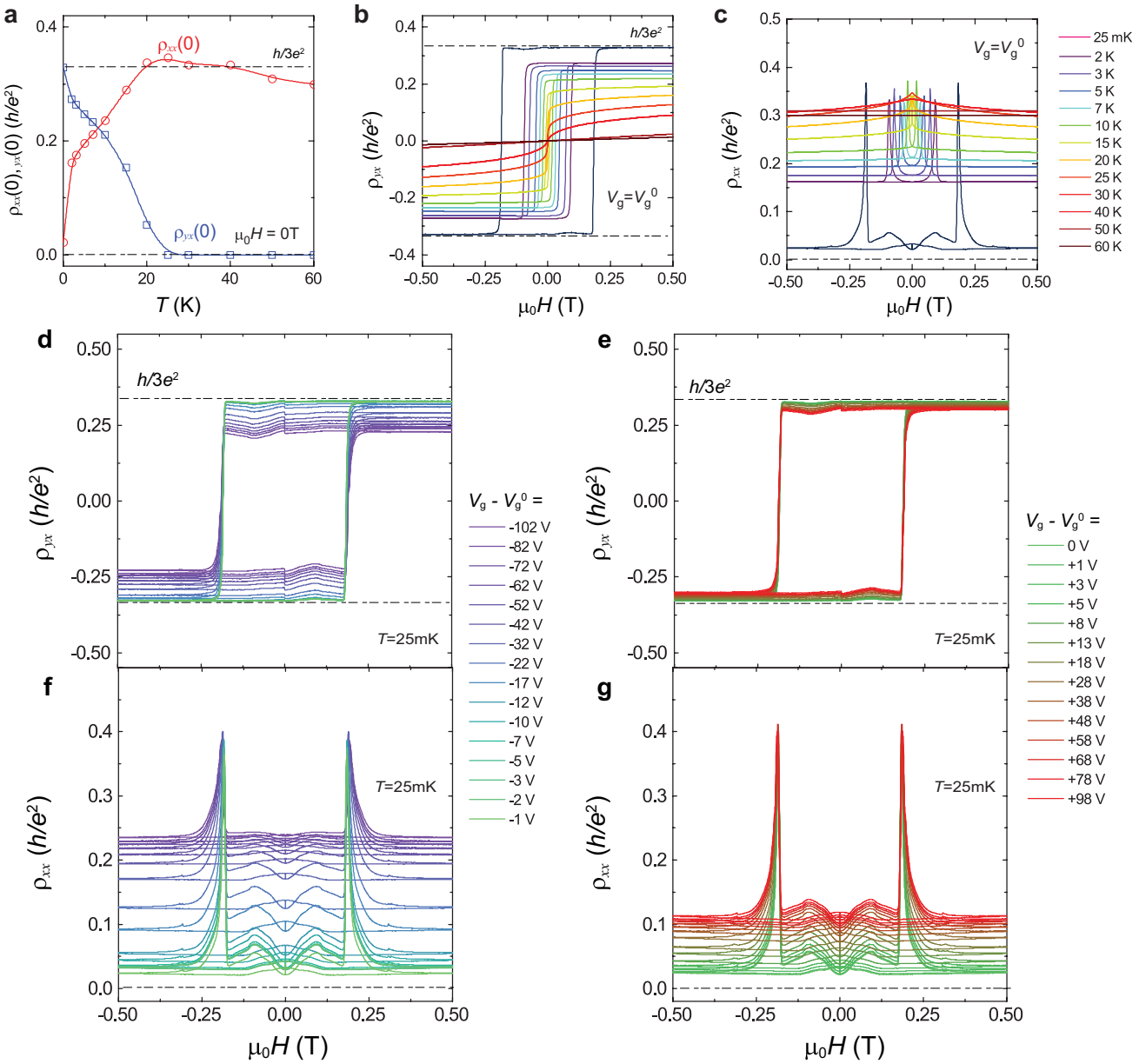

Extended Data Fig. 4 | Transport results for the $C = 3$ sample. As in Extended Data Fig. 2, but for the $C = 3$ sample.

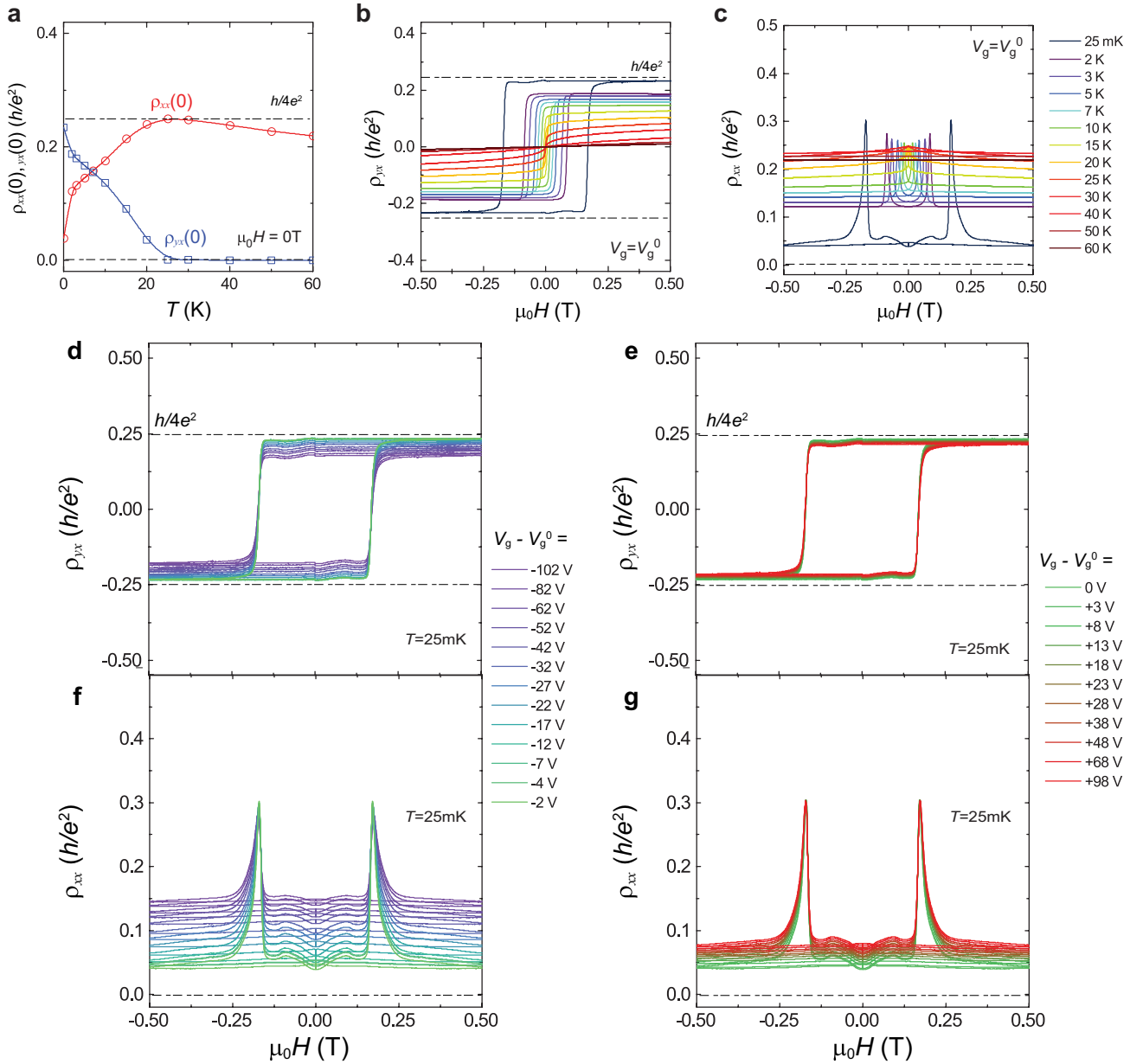

Extended Data Fig. 5 | Transport results of the $C = 4$ sample. As in Extended Data Fig. 2, but for the $C = 4$ sample.

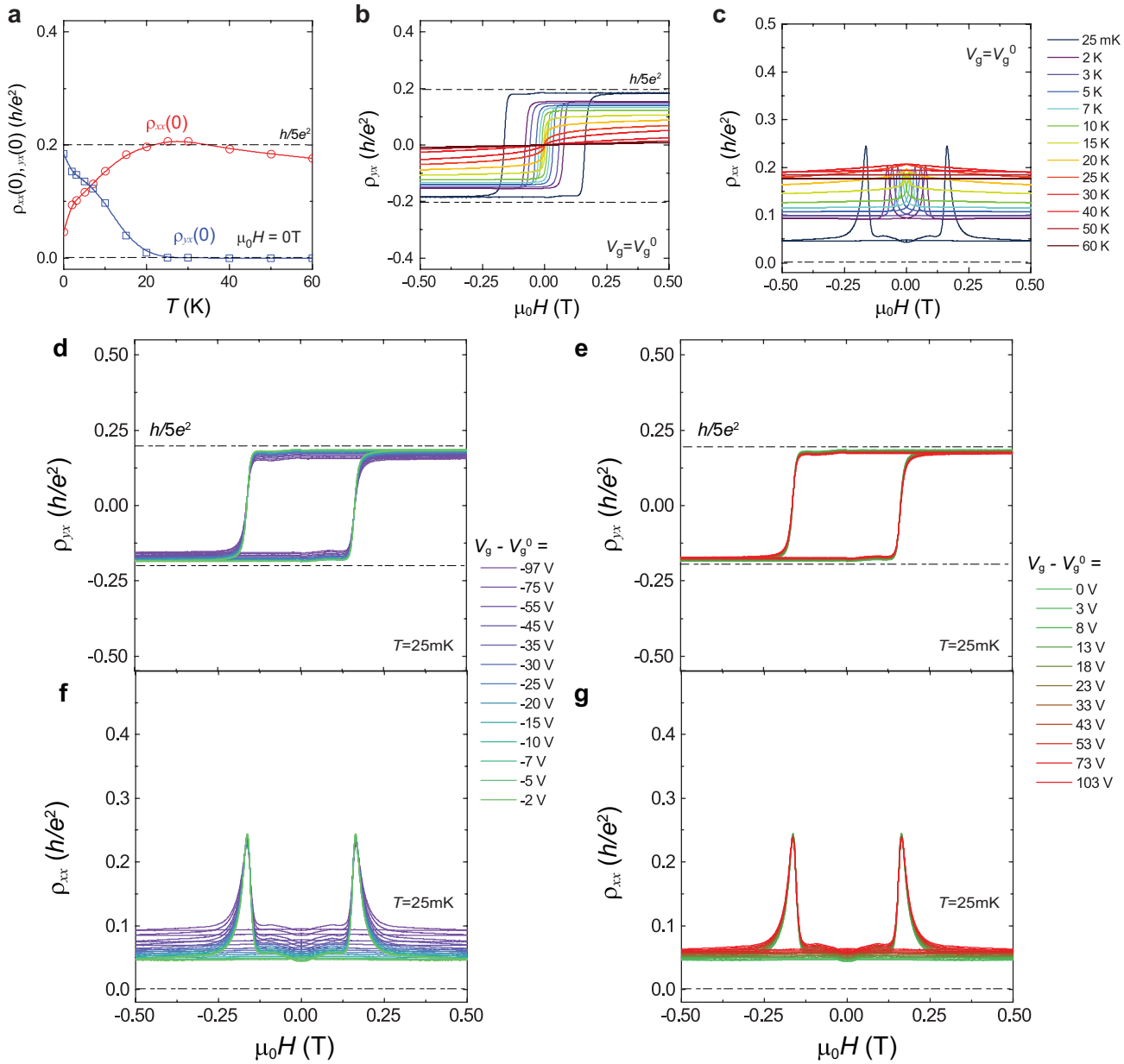

Extended Data Fig. 6 | Transport results of the $C = 5$ sample. As in Extended Data Fig. 2, but for the $C = 5$ sample.

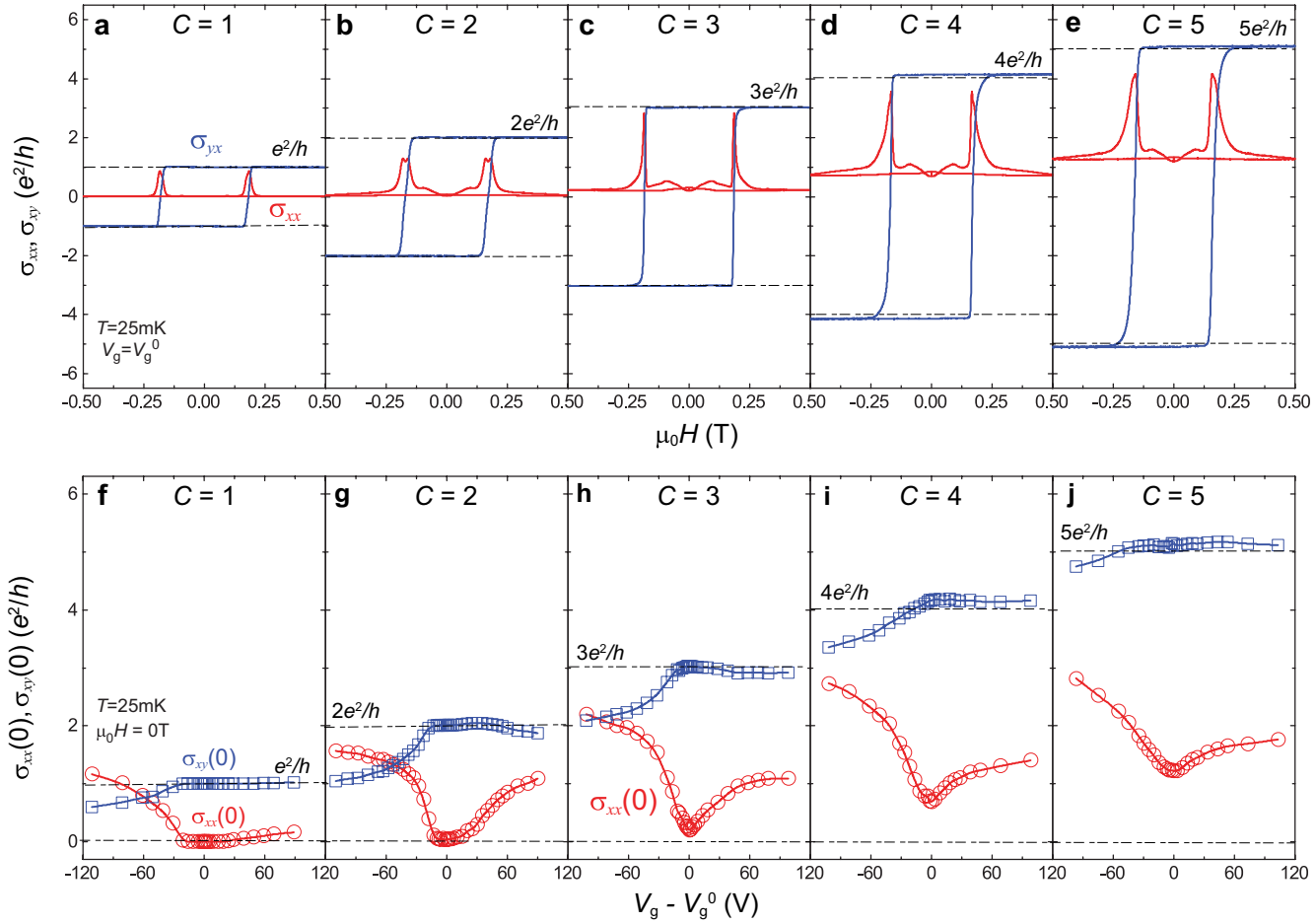

Extended Data Fig. 7 | Hall and longitudinal conductance results for the C = 1–5 samples. a–e, Dependence of the longitudinal conductance σ_{xx} (red) and Hall conductance σ_{xy} (blue) on $\mu_0 H$ for the C = 1–5 samples. All measurements were taken at the charge-neutral point ($V_g = V_{g,0}$) and T = 25 mK. **f–j**, Dependence of $\sigma_{xy}(0)$ (blue squares) and $\sigma_{xx}(0)$ (red circles) on gate voltage ($V_g - V_{g,0}$) for the C = 1–5 samples. All measurements were taken at T = 25 mK and $\mu_0 H$ = 0 T after magnetic training.

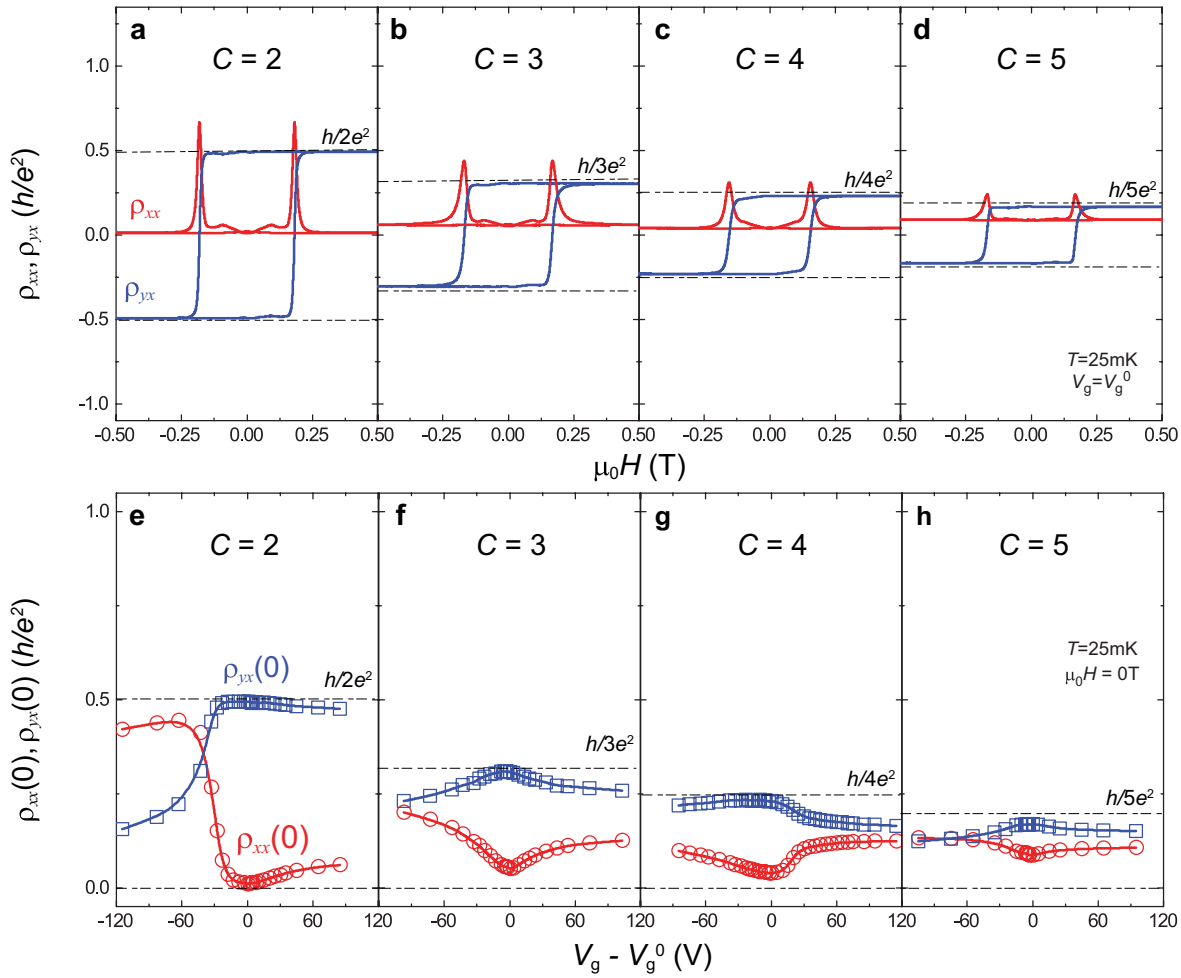

Extended Data Fig. 8 | The high-*C* QAH effect observed in another group of magnetic TI/TI multilayer samples. a–**d**, Dependence of ρ_{xx} (red) and ρ_{yx} (blue) on $\mu_0 H$, measured at the charge-neutral point ($V_g = V_{g,0}$) and $T = 25$ mK. $\rho_{yx}(0)$ displays the quantized values of $0.494h/e^2$, $0.307h/e^2$, $0.231h/e^2$ and $0.169h/e^2$ for the samples with $C = 2$, 3, 4 and 5, respectively. The corresponding $\rho_{xx}(0)$ values are $0.010h/e^2$, $0.050h/e^2$, $0.039h/e^2$ and $0.087h/e^2$. $V_{g,0}$ values for the four samples are +15 V ($C = 2$), −3 V ($C = 3$), −15 V ($C = 4$) and +5 V ($C = 5$). **e**–**h**, Dependence of $\rho_{yx}(0)$ (blue squares) and $\rho_{xx}(0)$ (red circles) on gate voltage ($V_g - V_{g,0}$) for the $C = 2$–5 samples. All measurements were taken at $T = 25$ mK and $\mu_0 H = 0$ T after magnetic training.

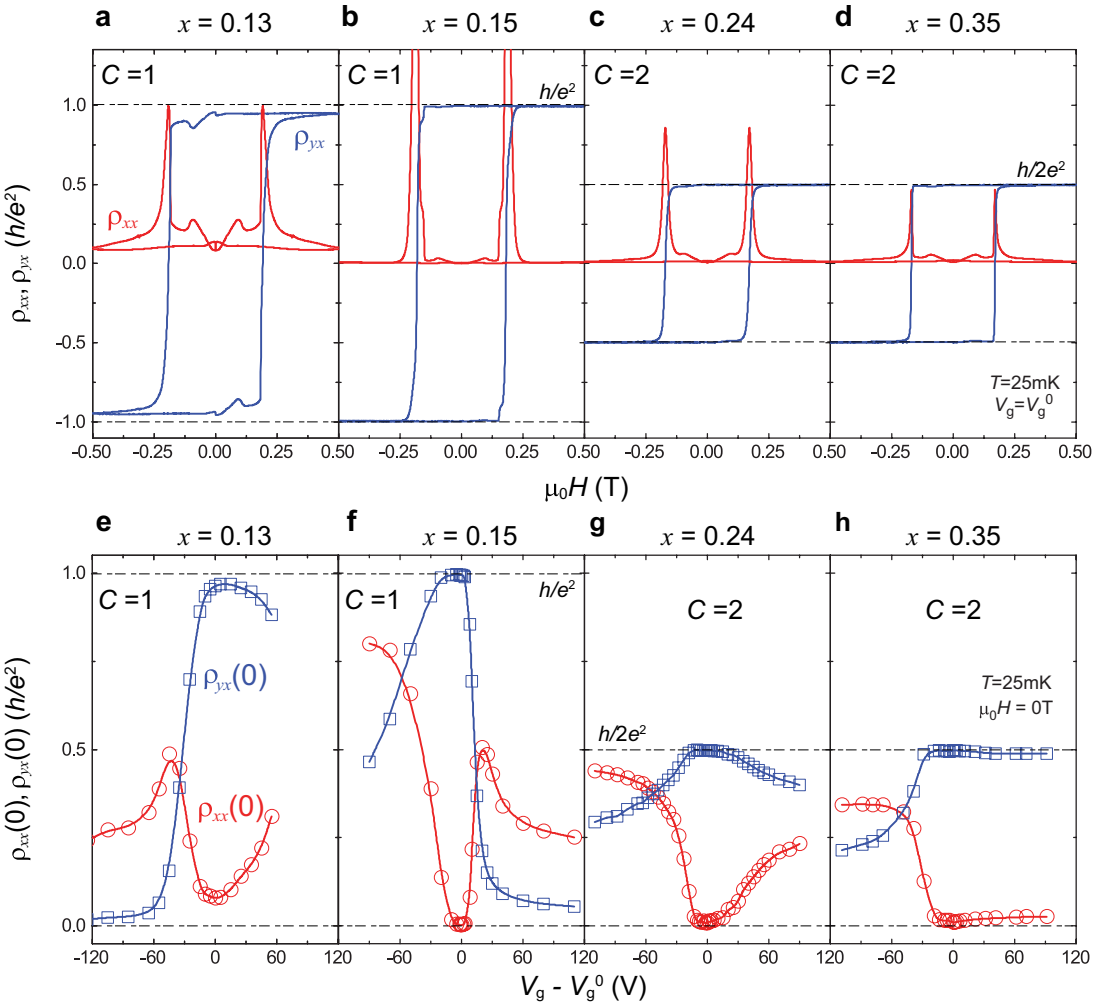

Extended Data Fig. 9 | Chern number tuned by varying the Cr doping level in magnetic TI layers. a–**d**, Dependence of ρ_{xx} (red) and ρ_{yx} (blue) on $\mu_0 H$ for the $m = 2$ sample, with different Cr doping levels x. All measurements were taken at the charge-neutral point ($V_g = V_{g,0}$) and $T = 25$ mK. $\rho_{yx}(0)$ displays the quantized values of $0.969h/e^2$, $0.994h/e^2$, $0.498h/e^2$ and $0.497h/e^2$ for the samples with $x = 0.13$, 0.15, 0.24 and 0.35, respectively. The corresponding $\rho_{xx}(0)$ value are $0.078h/e^2$, $0.002h/e^2$, $0.008h/e^2$ and $0.010h/e^2$. **e**–**h**, Dependence of $\rho_{yx}(0)$ (blue squares) and $\rho_{xx}(0)$ (red circles) on gate voltage ($V_g - V_{g,0}$) for $x = 0.13$, 0.15, 0.24 and 0.35. All measurements were taken at $T = 25$ mK and $\mu_0 H = 0$ T after magnetic training.

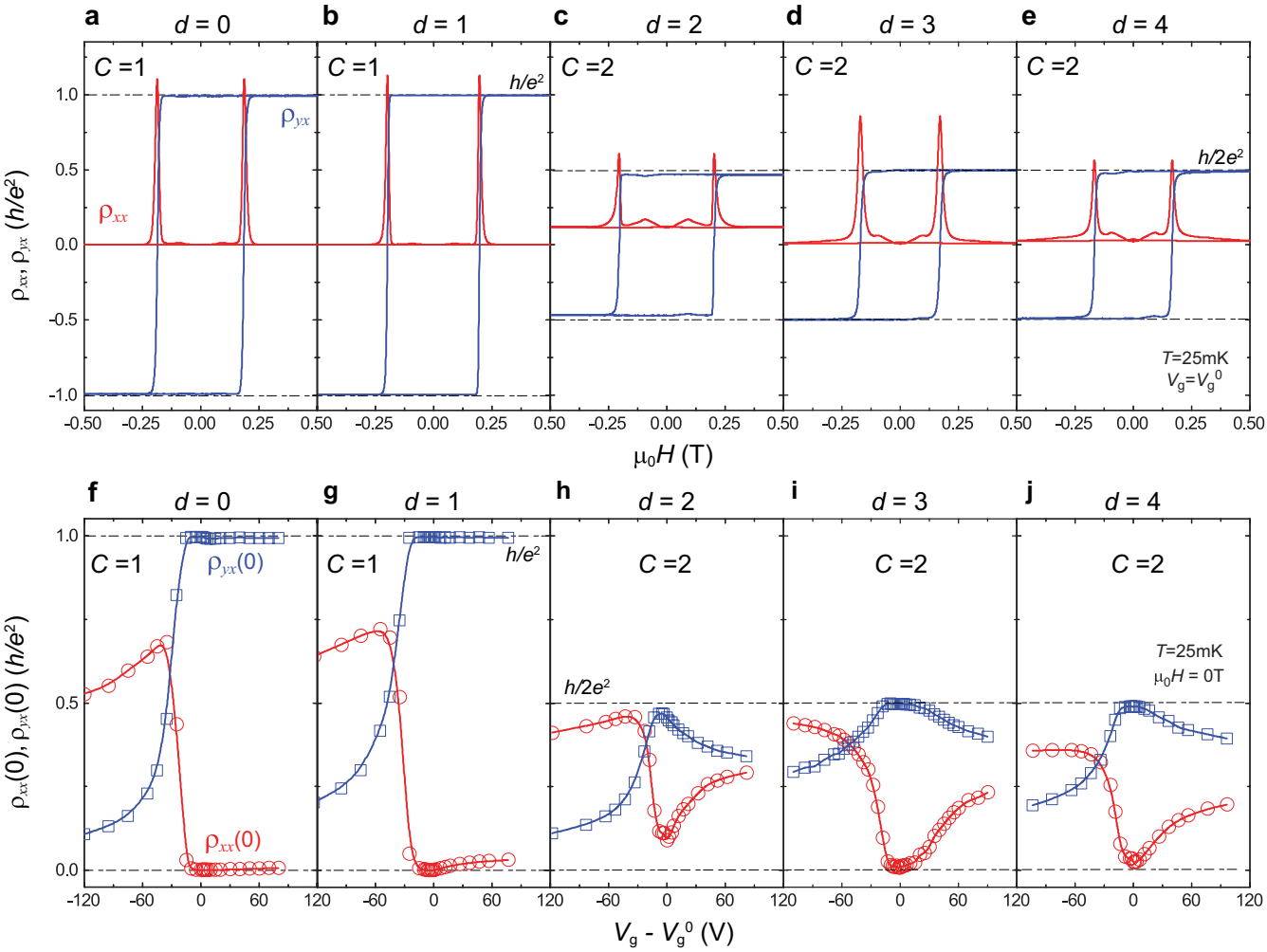

Extended Data Fig. 10 | Chern number tuned by controlling the thickness of the middle magnetic TI layer. a–d, Dependence of ρ_{xx} (red) and ρ_{yx} (blue) on $\mu_0 H$ for the $m = 2$ sample, with different middle magnetic TI layer thicknesses d. All measurements were taken at the charge-neutral point ($V_g = V_{g,0}$) and $T = 25$ mK. $\rho_{yx}(0)$ displays the quantized values of $0.995h/e^2$, $0.996h/e^2$, $0.469h/e^2$, $0.498h/e^2$ and $0.490h/e^2$ for the samples with $d = 0, 1, 2, 3$ and 4, respectively. The corresponding $\rho_{xx}(0)$ values are $0.0001h/e^2$, $0.0009h/e^2$, $0.089h/e^2$, $0.008h/e^2$ and $0.024h/e^2$. **e–h**, Dependence of $\rho_{yx}(0)$ (blue squares) and $\rho_{xx}(0)$ (red circles) on gate voltage ($V_g - V_{g,0}$) for $d = 0, 1, 2, 3$ and 4. All measurements were taken at $T = 25$ mK and $\mu_0 H = 0$ T after magnetic training. Because the $d = 2$ sample is near the topological phase transition regime and therefore has a smaller hybridization gap (Fig. 4d), it has a larger ρ_{xx}. For the $d = 4$ sample, the larger ρ_{xx} is probably induced by the enhanced dissipative quasi-helical side surface states and/or residual bulk carriers with increasing sample thickness.